



## Effect of cation size of binary cation ionic liquid mixtures on capacitive energy storage

Anna Seltmann<sup>a,b</sup>, Taras Verkholyak<sup>c</sup>, Dariusz Gołowicz<sup>d</sup>, Emmanuel Pameté<sup>a</sup>,  
Andrij Kuzmak<sup>e</sup>, Volker Presser<sup>a,b,f</sup>, Svyatoslav Kondrat<sup>d,g,\*</sup>

<sup>a</sup> INM – Leibniz Institute for New Materials, Campus D2 2, 66123, Saarbrücken, Germany

<sup>b</sup> Saarland University, Campus D2 2, 66123, Saarbrücken, Germany

<sup>c</sup> Institute for Condensed Matter Physics, National Academy of Sciences of Ukraine, 79011 Lviv, Ukraine

<sup>d</sup> Institute of Physical Chemistry, Polish Academy of Sciences, 01-224 Warsaw, Poland

<sup>e</sup> Department for Theoretical Physics, I. Franko National University of Lviv, 79005 Lviv, Ukraine

<sup>f</sup> Saarene – Saarland Center for Energy Materials and Sustainability, Campus C4 2, 66123, Saarbrücken, Germany

<sup>g</sup> Institute for Computational Physics, University of Stuttgart, 70569 Stuttgart, Germany

### ABSTRACT

Ionic liquid mixtures show promise as electrolytes for supercapacitors with nanoporous electrodes. Herein, we investigate theoretically and with experiments how binary electrolytes comprising a common anion and two types of differently-sized cations affect capacitive energy storage. We find that such electrolytes can enhance the capacitance of single nanopores and nanoporous electrodes under potential differences negative relative to the potential of zero charge. For a two-electrode cell, however, they are beneficial only at low and intermediate cell voltages, while a neat ionic liquid performs better at higher voltages. We reveal subtle effects of how the distribution of pores accessible to different types of ions correlates with charge storage and suggest approaches to increase capacitance and stored energy density with ionic liquid mixtures.

### 1. Introduction

Electrical double-layer capacitors (EDLCs), also called supercapacitors or ultracapacitors, play an important role in sustainable energy storage [1–4] and open new opportunities for energy harvesting [5–9]. EDLCs store energy by the voltage-induced adsorption of ionic charge into the pores of their electrodes. Since this process typically does not involve chemical reactions, EDLCs provide high power densities and cycling stability, but the stored energy densities are moderate compared to conventional batteries [1,10]. Enhancing energy storage has therefore been identified as one of the main directions in the supercapacitor research [2,10] aimed at making these ecologically-friendly energy storage devices more widely applicable in industry and everyday life.

Ionic liquid (IL) mixtures are promising electrolytes for increasing storage capacity [11–13] and thermal stability [14] of EDLCs and avoiding the energy-power trade-off in their performance [11]. For instance, Wang et al. [11] studied experimentally and with classical density functional theory (DFT) and simulations a mixture of 1-ethyl-3-methylimidazolium tetrafluoroborate ([EMIM][BF<sub>4</sub>]) and tetramethylammonium tetrafluoroborate ([TMA][BF<sub>4</sub>]) and reported a simultane-

ous enhancement of capacitance and charging dynamics, though the effect was relatively moderate, amounting to about 10% to 30% enhancement in the capacitance. These authors found that the capacitance increased in mesopores (pore widths between 2 nm to 50 nm) but decreased in micropores (pores smaller than 2 nm), which they related to the differences in the adsorption of [EMIM] and [TMA] cations into micro and mesopores [11]. Neal et al. [12] considered a primitive model of electrolyte consisting of a common cation and differently sized anions. Using DFT, they revealed a non-monotonic relationship between the integral capacitance of slit micropores and the molar fraction of the smaller anion. In a more recent work, Cats and van Roij [13] employed DFT to study a similar electrolyte in slit mesopores and found that the smaller anion determines the charging behaviour under positive potentials applied to the pore with respect to the bulk electrolyte. Yambou et al. [14] studied experimentally a more complex IL mixture based on the [EMIM] cation and bis(fluorosulfonyl)imide ([FSI]), [BF<sub>4</sub>], and tetracyanoborate ([TCB]) anions, demonstrating that such electrolytes could be beneficial for energy storage at low temperatures (down to –50 °C), though they performed comparably to simple and binary electrolytes when the temperature was raised.

\* Corresponding author.

E-mail addresses: [svyatoslav.kondrat@gmail.com](mailto:svyatoslav.kondrat@gmail.com), [skondrat@ichf.edu.pl](mailto:skondrat@ichf.edu.pl) (S. Kondrat).

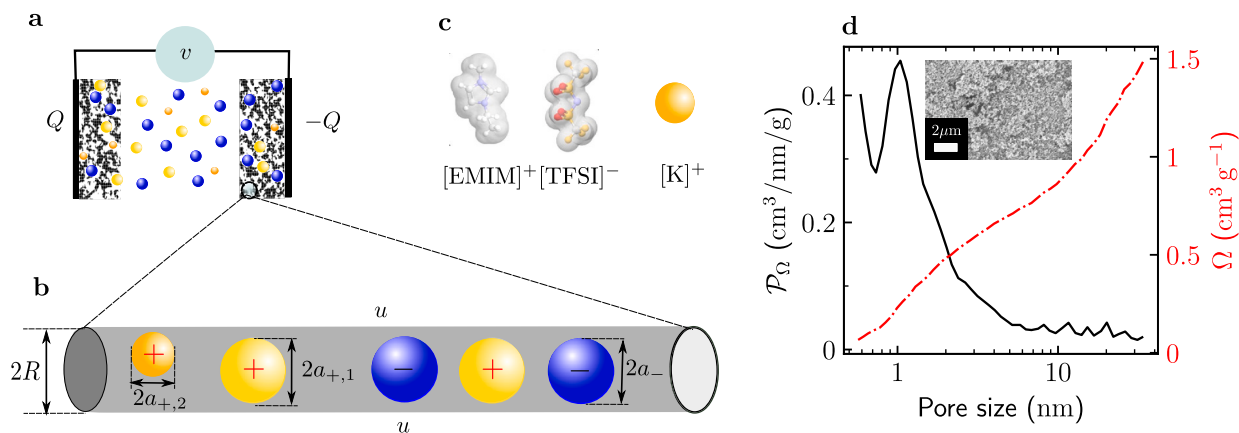


**Fig. 1.** EDLCs with a binary cation IL mixture and nanoporous electrodes. (a) Schematic of an EDLC consisting of a binary electrolyte sandwiched between nanoporous electrodes. Cell voltage  $v$  is applied between the two electrodes, leading to charges  $Q_1 = Q$  and  $Q_2 = -Q$  on the positive and negative electrodes. (b) Schematic of a single-file pore of radius  $R$  filled with a binary cation electrolyte. Ions are modelled as charged hard spheres. All anions have the same radius  $a_-$ , while cations can have different radii  $a_{+,1} \neq a_{+,2}$ . Potential difference  $u$  is applied to the pore with respect to the bulk electrolyte. (c) Schematic of [EMIM][TFSI] ionic liquid and a potassium cation used in our experiments (Section 2.2.2). (d) Differential ( $P_\Omega$ ) and cumulative ( $\Omega$ ) pore size distributions of activated carbon black (Section 2.2.1). The inset shows an electron micrograph of the electrode matrix.

These reports demonstrate the potential of using IL mixtures in supercapacitor applications. However, understanding charge storage mechanisms with such electrolytes and their relation to the electrode structure is still lacking. In this article, we use theoretical modelling and electrochemical experiments to investigate electrolytes based on a common anion and two differently-sized cations. We use a computationally efficient exactly-solvable model [15], which allows us to systematically investigate the relation among ion sizes, electrolyte composition, pore sizes and their distribution in the supercapacitor electrodes. We find that such electrolytes can enhance capacitance of single nanopores and nanoporous electrodes but perform moderately for EDLC devices consisting of two electrodes. We discuss the origin of these limitations and possibilities for increasing capacitive energy storage with IL mixtures.

## 2. Methods

### 2.1. Theoretical

We consider an EDLC consisting of two electrolyte-filled nanoporous electrodes separated by a sufficiently large bulk reservoir, with a cell voltage  $v$  applied between the electrodes (Fig. 1a). We assume that the electrodes consist of cylindrical nanopores of (in general) different radii  $R$  but sufficiently narrow to accommodate only a single file of ions. Verkholyak et al. mapped this system onto a one-dimensional (1D) off-lattice model of interacting particles with an exact analytical solution for the voltage-dependent in-pore ion densities, showing a quantitative agreement with the results of Monte Carlo simulations of the full (three-dimensional) model [15]. Although slit pore models, which are often used to determine a pore-size distribution of nanoporous electrodes [16] (Section 2.2.1), might be a more realistic representation of nanoporous electrodes, the analytical solution for single-file pores provides a convenient and computationally inexpensive tool enabling a systematic study of EDLC's charging.

For an electrolyte, we take an ionic fluid consisting of a common anion of radius  $a_- = 0.25$  nm and two types of cations of different radii  $a_{+,1} = a_-$  and  $a_{+,2} \neq a_{+,1}$ . We consider  $a_{+,2} = 0.15$  nm  $<$   $a_{+,1}$  and  $a_{+,2} = 0.3$  nm  $>$   $a_{+,1}$  and investigate how the EDLC energy storage capabilities depend on the fraction of the second cation in the electrolyte. We model all ions as monovalent charged hard spheres. Such models have been ubiquitously used [4] to study ILs [17–26] and IL mixtures [12,27,28]. We denote by  $\rho_1 = \rho_{+,1}$  and  $\rho_2 = \rho_{+,2}$  the bulk densities of the first (reference) and second ion pairs, respectively, so that the total density of ion pairs in the bulk electrolyte is  $\rho = \rho_- = \rho_1 + \rho_2$ . Corre-

spondingly, the total bulk ion density is  $2\rho$  and the molar concentrations of the first and second ion pairs are  $x_1 = \rho_1/\rho$  and  $x_2 = 1 - x_1 = \rho_2/\rho$ , respectively.

In equilibrium, electrochemical potentials of ions in the bulk and inside the pores are equal. Thus, to determine the equilibrium in-pore ion densities, we need the bulk (electro)chemical potentials  $\mu_\alpha$  ( $\alpha \in \{(+, 1); (+, 2); -\}$ ), which depend on the bulk ion densities, temperature, and pressure. We first describe the method we used to compute  $\mu_\alpha$  and then discuss the model employed to calculate the in-pore ion densities.

#### 2.1.1. Bulk chemical potentials of ion pairs

The bulk chemical potentials of ions,  $\mu_\alpha$ , contain the ideal and excess parts. To calculate the latter, we used Widom's insertion method [29], in which a particle or a group of particles is inserted into a simulation box to compute the energy change  $\Delta\mathcal{E}$  in the simulation system; the average of  $\exp(-\beta\Delta\mathcal{E})$ , where  $\beta = (k_B T)^{-1}$  with  $k_B$  being the Boltzmann constant and  $T$  temperature, can be related to the excess chemical potential [29]. We used the Espresso MD package (<https://github.com/espressomd>) [30], which offers an open source implementation of this method along with molecular dynamics (MD) simulations. We inserted ion pairs to keep the system electroneutral, thus computing the excess chemical potential of ion pairs

$$\mu_i^{\text{ex}} = \mu_{+,i}^{\text{ex}} + \mu_-^{\text{ex}}. \quad (1)$$

In this way, we obtain two chemical potentials  $\mu_1^{\text{ex}}$  and  $\mu_2^{\text{ex}}$  for an electrolyte containing a common anion and two different cations. To fully characterise the system, one needs an additional combination of (electro)chemical potentials, which we related to the potential of zero charge for ions in a nanopore or electrode (Sections 2.1.3 and 2.1.4).

In all simulations, the total number of ions was  $N = 200$  and the simulation box length  $L \approx 5.5$  nm for all electrolyte compositions. These values of  $N$  and  $L$  correspond to the bulk concentration  $\rho_b = 1$  M, typical for EDLCs [6,31]. To mimic the hard-core interactions between the ions, we used the generic Lennard-Jones interaction potential with exponents 50 and 49 and the potential depth  $\beta\epsilon_{\text{HS}} = 1.5$  [32]. We took a background relative dielectric constant  $\epsilon_r = 20$ , which describes the dielectric permittivity of bulky ions or weakly polar solvent (for simplicity, and in the absence of simple theory, we follow other publications [6,9] and ignore its dependence on the pore size and ion density). The total number of iterations was  $10^5$ , with  $10^3$  Widom insertions and  $10^4$  MD steps per iteration.

In addition to fixing the total ion concentration when varying the electrolyte composition (*i.e.*,  $x_2$ ), as described above, we also performed

calculations for a constant bulk pressure. We first computed the pressure for  $x_2 = 0$  and then determined the equilibrium simulation box lengths for each molar fraction  $x_2$  providing the same pressure. To this end, we conducted MD simulations of the same model in NPT ensemble with the LAMMPS simulation package [33] (<https://www.lammps.org>). Before starting a series of NPT runs, we equilibrated the  $x_2 = 0$  system in NVT ensemble for 150 ns (5 fs step) using Nosé–Hoover thermostat provided by LAMMPS. We used the generic Lenard-Jones potential and the system parameters as described above in this section. The computed pressure of the equilibrated  $x_2 = 0$  system was approximately 67.73 bar (such high pressures are typical and result from the absence of attractive dispersion interactions). We next ran NPT simulations with the Nosé–Hoover barostat and thermostat for the systems with  $x_2 = 0, 0.2, 0.4, 0.6, 0.8,$  and  $1$  at the same pressure. Each NPT run was 150 ns long (5 fs step). We calculated the box size for each equilibrated system and then performed MD simulations with the Widom insertion as described above using the same parameters except for the box sizes.

The total bulk chemical potential  $\mu_i$  of ion pair  $i$  is a sum of the ideal-gas and excess parts. The results for  $\mu_i$  are shown in Figs. S1 and S2.

### 2.1.2. Single-file pores: mapping to a 1D model and its analytical solution

We describe an ionic system inside a single-file nanotube using a grand canonical ensemble, with the concentration of each component determined by the bulk chemical potential of ions (along with the temperature, nanotube and ion radii, and potential difference  $u$  applied to a nanopore relative to the bulk electrolyte). Its mapping onto a 1D system of interacting hard-core particles can be done by associating the ion positions along the cylinder main axis with the ion coordinates in the 1D model and integrating out the degrees of freedom in the remaining two directions. This procedure leads to a shift in the electrochemical potentials of ions in the 1D model [15],

$$\tilde{\mu}_\alpha^{1D} = \tilde{\mu}_\alpha^{3D} - \tilde{\psi}_\alpha, \quad (2)$$

where  $\tilde{\mu}_\alpha^{3D}$  is the electrochemical potential of species  $\alpha$  in a 3D nanopore (which in equilibrium is equal to the bulk chemical potential  $\mu_\alpha$ ), and

$$\beta\tilde{\psi}_\alpha = -\ln \left( 2\pi \int_0^{R_a - a_\alpha} e^{-\beta\psi_\alpha(r)} r \, dr \right) \quad (3)$$

results from integrating over the degrees of freedom perpendicular to the nanopore symmetry axis [15]. In Eq. (3),  $\psi_\alpha(r)$  is the interaction energy of ion  $\alpha$  with the nanotube wall. In this work, we consider steric and image charge interactions (Section S1 B in the Supplementary Material) and neglect dispersion forces.  $R_a = R - a_c$  is the accessible pore radius, where  $a_c$  is the radius of the wall atom (in all calculations, we took  $a_c = 0.1685$  nm, which corresponds to the radius of carbon atom). The upper limit in the integral in Eq. (3) ensures hard-core exclusion between an ion and the pore wall. Following our previous work [9,15,34], we included the thermal de Broglie wavelength in  $\tilde{\mu}_\alpha^{3D}$ , whose contribution is identical in the bulk and in the pore.

The electrostatic interactions between ions inside a conducting nanotube are screened by the charge carriers (electrons and holes) on the nanotube walls [35–38]. For an ideally metallic nanotube, this screening is exponential with the leading-order decay length determined by the nanotube radius [37,38]; we present the corresponding interaction potential in Section S1 A in the Supplementary Material. Quantum density functional calculations suggest [39–41] that this interaction potential provides a reliable approximation also for gold and carbon nanotubes (CNTs). However, a finite density of states (DOS) of CNT walls leads to a finite quantum capacitance  $C_q$  ( $C_q = \infty$  for ideally metallic pores) [42], which tends to reduce the total (measured) capacitance [43–46] and may give rise to interesting effects such as an energy storage enhancement at high applied potential differences [34]. In this work, we neglect these effects and note that we expect a similar qualitative behaviour as discussed below also for CNTs and other

carbon-based electrodes provided the in-pore ions do not significantly modify their DOS [47].

The exponential screening of in-pore ion-ion interactions allows one to neglect the interactions beyond nearest-neighbour ions in single-file pores. For a one-dimensional system of particles interacting only with their nearest neighbours, one can analytically calculate the equilibrium particle densities for given electrochemical potentials, temperature, and interaction energy (which depends on the pore radius) [15,48]. The details of these calculations and the resulting expressions are presented in Section S2 in the Supplementary Material.

### 2.1.3. Electrochemical potentials of ions and a one-electrode setup

The electrochemical potentials of ions can be presented as ( $i = 1, 2$ )

$$\tilde{\mu}_{+,i}^{1D} = \mu_{+,i}^{1D} + eu, \quad (4)$$

$$\tilde{\mu}_{-,i}^{1D} = \mu_{-,i}^{1D} - eu, \quad (5)$$

where  $\mu_\alpha^{1D}$  is the corresponding chemical potential,  $e$  is the proton charge and  $u$  is the electrostatic potential measured with respect to the bulk electrolyte. From MD simulations (Section 2.1.1) and using Eqs. (2) and (3), we obtain chemical potentials of ion pairs; correspondingly, we use

$$\tilde{\mu}_i^{1D} = \tilde{\mu}_{+,i}^{1D} - \tilde{\mu}_{-,i}^{1D} = \mu_{+,i}^{1D} + \mu_{-,i}^{1D}. \quad (6)$$

Since our electrolyte consists of three types of ions, we need an additional electrochemical potential or a combination of electrochemical potentials to characterize the ionic system; we chose

$$\Delta\tilde{\mu}^{1D} = \frac{1}{2N} \sum_{i=1}^N (\tilde{\mu}_{+,i}^{1D} - \tilde{\mu}_{-,i}^{1D}) = \frac{1}{2N} \sum_{i=1}^N (\mu_{+,i}^{1D} - \mu_{-,i}^{1D}) + eu = \Delta\mu^{1D} + eu, \quad (7)$$

where  $N$  is the number of different types of ion pairs (in our case  $N = 2$ , except for  $x_2 = 0$  and  $x_2 = 1$  when  $N = 1$ ). For a symmetric IL,  $\tilde{\mu}_{+,i}^{1D} = \tilde{\mu}_{-,i}^{1D}$  and hence  $\Delta\mu^{1D} = -eu$  is determined solely by the applied potential difference  $u$ . For asymmetric ILs, we computed the electrode charge  $Q$  (the negative of the ionic charge accumulated in the electrode pores) as a function of  $\Delta\mu^{1D}$  and determined  $\Delta\mu_0^{1D}$  as a solution of  $Q(\Delta\mu^{1D}) = 0$ , which defines the potential of zero charge (PZC)  $u_{PZC} = (\Delta\tilde{\mu}^{1D} - \Delta\mu_0^{1D})/e$ . We cannot determine the value of  $u_{PZC}$  without knowing  $\Delta\tilde{\mu}^{1D}$ , as it depends on the electrochemical potentials of individual species  $\tilde{\mu}_{+,i}^{1D}$  and  $\tilde{\mu}_{-,i}^{1D}$ . Therefore, we measure the applied potential difference with respect to  $u_{PZC}$ , that is, we present all results for a single nanotube or electrode as functions of  $u - u_{PZC}$ .

### 2.1.4. Averaging over a pore size distribution

A distribution of pores in an electrode can be measured experimentally through gas adsorption isotherms [49] or computed numerically for model porous materials using, e.g., the Gelb-Gubbins method [50]. Both methods provide a cumulative pore volume  $\Omega(\ell)$  defined as a volume of pores of sizes  $\ell$  and smaller. Note that  $\ell$  is the accessible pore size so that for a cylindrical pore  $\ell = 2R_a$ . The pore size distribution is conventionally defined as [51]  $P_\Omega = -d\Omega/d\ell$ ; the quantity  $P_\Omega(\ell)d\ell$  gives the volume of pores of sizes between  $\ell$  and  $\ell + d\ell$ . Fig. 1d shows differential and cumulative PSDs of activated carbon black used in our experiments (Section 2.2.1).

As discussed in Ref. [19], the relevant distribution function for averaging capacitance and energy density is the normalised distribution of the number of pores of size  $\ell$ :

$$P_n(\ell) = \frac{\omega^{-1}(\ell)P_\Omega(\ell)}{\int_0^\infty d\ell \omega^{-1}(\ell)P_\Omega(\ell)}, \quad (8)$$

where  $\omega(\ell)$  is the volume of a pore of width  $\ell$ . For a cylindrical pore of width (= diameter)  $\ell$  and length  $H$ , the volume  $\omega(\ell) = \pi H \ell^2/4$ , while for slit pores  $\omega(\ell) = H^2 \ell$ . Examples of  $P_n(\ell)$  for activated carbon black assuming slit and cylindrical pores are shown in Fig. S3.

With  $\mathcal{P}_n(\ell)$  at hand, one performs averaging of any  $\ell$ -dependent quantity  $A$  as usual

$$\langle A \rangle_{\mathcal{P}_n} = \int_0^\infty d\ell \mathcal{P}_n(\ell) A(\ell). \quad (9)$$

We used Eq. (9) to compute the electrode charge and capacitance,  $\langle Q(\Delta\mu^{1D}) \rangle_{\mathcal{P}_n}$  and  $\langle C(\Delta\mu^{1D}) \rangle_{\mathcal{P}_n}$ , where  $\Delta\mu^{1D}$  follows from Eq. (7). To compute the potential of zero charge, we solved numerically the equation  $\langle Q(\Delta\mu^{1D}) \rangle_{\mathcal{P}_n} = 0$ , similarly as for a single nanopore.

### 2.1.5. Two-electrode cell

Under applied cell voltage  $v$ , the equilibrium charge on two electrodes of an EDLC must be equal in absolute value and opposite in sign, *i.e.*

$$Q_1(u_1) = -Q_2(u_2), \quad (10)$$

where  $u_1$  [ $u_2$ ] is the potential at the first [second] electrode with respect to the potential of the bulk electrolyte so that  $v = u_1 - u_2$ . To find  $u_1$ , we solved Eq. (10) numerically with `fsolve` routine from the `SciPy` python package using the data for  $Q(\Delta\mu^{1D})$  calculated for a given electrode in a single electrode setup. We differentiated numerically  $Q(v) = Q_1(u_1)$  with respect to  $v$  to compute the total capacitance of a two-electrode cell.

## 2.2. Experimental

### 2.2.1. Nanoporous electrodes

Commercial highly-porous carbon black (BP2000 from Cabot) was used to prepare the electrodes for supercapacitors. First, 95 mass% of the active material (BP2000) was mixed with 10 mass% of binder (polytetrafluoroethylene, 60 mass% dispersion in water, Sigma Aldrich) within a mortar, and the mixture was trituated until a homogeneous dough was obtained. Next, the obtained dough was rolled with a calendaring machine (HR01 hot rolling machine, MTI) to form a  $(250.0 \pm 0.6)$   $\mu\text{m}$  thick sheet, from which electrodes disk of 11 mm diameter were punched out and dried at 120 °C for 12 h under vacuum at 60 mbar. The electrode density was  $(0.29 \pm 0.05)$   $\text{g cm}^{-3}$ .

The analysis of nitrogen sorption at 77 K was conducted using a Quadrasorb IQ system (formerly Quantachrome, now Anton Paar) to investigate the porous structure of PTFE-bound electrodes. Before the measurements, the electrodes were degassed for 12 h at 100 °C under vacuum conditions. Porosity analysis was performed using a two-dimensional non-local density functional theory, assuming a slit-shaped pore configuration. The resulting cumulative and differential distribution of pores is shown in Fig. 1d.

A ZEISS GEMINI 500 scanning electron microscope (SEM) was used to determine the carbon material micrograph (the inset in Fig. 1d) by applying an accelerating voltage of 1 kV at a working distance of 4.5 mm. For the measurements, the samples were mounted on an aluminum stub fixed with copper tape.

### 2.2.2. Electrolytes

A mixture of IL electrolyte was prepared by dissolving potassium trifluoromethanesulfonimide ( $[\text{K}][\text{TFSI}]$ ; >99%, Iolitec) salt in a dried 1-ethyl-3-methylimidazolium-bis(trifluoromethylsulfonyl)imide ( $[\text{EMIM}][\text{TFSI}]$ ; >99%, Iolitec) in 1:9 molar ratio ( $[\text{K}]_{0.1}[\text{EMIM}]_{0.9}[\text{TFSI}]$ ). The mixture was stirred inside a glovebox (MBraun,  $\text{H}_2\text{O} < 0.1$  ppm, and  $\text{O}_2 < 0.1$  ppm) under an argon atmosphere and used as an electrolyte in the supercapacitor cell assembly. The ionic conductivity of each electrolyte was assessed following the procedure described in [52] by utilizing a Microcell HC electrochemical cell (RHD Instruments) equipped with Pt electrodes. We obtained at 25 °C the following values:  $8.7 \mu\text{S cm}^{-1}$  for pure  $[\text{EMIM}][\text{TFSI}]$  and  $5.1 \mu\text{S cm}^{-1}$  for  $[\text{K}]_{0.1}[\text{EMIM}]_{0.9}[\text{TFSI}]$ . The measurements were conducted using a Modulab electrochemical workstation with ESC software (Solartron Analytical).

First, 400  $\mu\text{L}$  of each electrolyte was carefully injected into the measuring cup into the glove box. Subsequently, the Pt electrode crucible was securely sealed. The closed cell was then affixed to the Peltier element of a temperature-controlled base unit (Eurotherm 2000) using heat sink paste to enhance heat transfer between the Peltier element and the crucible. After allowing 10 min for temperature stabilization, potentiostatic impedance was at a standard temperature of 25 °C. The impedance measurements were performed over a frequency range from 700 kHz to 1 Hz at open circuit potential. To determine the cell constant  $K_{\text{cell}}$ , the conductance obtained from a 0.1 M potassium chloride (KCl) aqueous standard (VWR) with a known conductivity of  $12.88 \text{ mS cm}^{-1}$  at 25 °C was utilized, employing the following equation:

$$G = \frac{A}{l} \sigma = K_{\text{cell}} \sigma, \quad (11)$$

where  $G$  is the conductance,  $A$  is the area of the electrode surface,  $l$  the height of the electrolyte level, and  $\sigma$  is the conductivity. The cell constant was obtained using the impedance data for different temperatures of the 1 M KCl solution with a known conductivity of  $12.88 \text{ mS cm}^{-1}$  at 25 °C.

### 2.2.3. Electrochemical measurements

For electrochemical investigations, we used two-electrode polyethylene-ether-ketone (PEEK) cells equipped with spring-loaded titanium pistons [45]. The cells were assembled using a glass microfiber membrane (GF/A, Whatman) as a separator sandwiched between two carbon electrodes soaked with the IL electrolyte. All electrochemical measurements were done at  $(25 \pm 1)$  °C in a climate chamber (Binder) using a potentiostat/galvanostat (Bio-Logic VMP300) controlled with EC-Lab software. Cyclic voltammetry (CV) at different scan rates ( $2 \text{ mV s}^{-1}$  to  $500 \text{ mV s}^{-1}$ ), galvanostatic cycling with potential limitation (GCPL, at  $200 \text{ mA g}^{-1}$ ), and electrochemical impedance spectroscopy (EIS, at 0 V with a sinusoidal signal of 5 mV in the frequency range from 100 kHz to 1 MHz) were carried out in the voltage range from 0 to 3 V. The specific capacitance  $C_s$  (in  $\text{F g}^{-1}$ ) was calculated by using the following equation:

$$C_s = \frac{2It_{\text{dis}}}{m_s U_{\text{max,corr}}}, \quad (12)$$

where  $t_{\text{dis}}$  (s) is the discharge time,  $I$  (mA) is the applied current,  $m_s$  (mg) is the mass of the electrode, and  $U_{\text{max,corr}}$  (V) is the maximum cell potential corrected from the ohmic drop. For a better comparison of experimental and theoretical results, the areal capacitance values were calculated by dividing the specific capacitance by the specific surface area of the BP2000 carbon electrode. Accordingly, the energy efficiencies (EE) were determined by integrating the charge and discharge areas of the GC/GD as a function of time:

$$\text{EE} = 100 \frac{\int_D U(t) dt}{\int_C U(t) dt}, \quad (13)$$

where  $C$  and  $D$  denote charge and discharge parts of the GC/GD curve (*cf.* Fig. 6b).

## 3. Results and discussions

In our theoretical calculations and experiments, we consider an electrolyte containing cations and anions of comparable sizes and investigate how the capacitive properties of nanoporous electrodes and EDLCs change when we mix this electrolyte with an ionic fluid having the same anion but a differently-sized cation. We first address this problem theoretically using a model of single-file nanopores (Fig. 1b). The analytical solution for the ion densities inside such pores (Section 2.1.2) allowed us to investigate the capacitance-electrolyte-pore size relations in detail (Section 3.1). In Section 3.2, we use this analytical solution to study charging of a single nanoporous electrode, and in Section 3.3, we consider a two-electrode EDLC. We then present our experimental results for EDLCs using pure  $[\text{EMIM}][\text{TFSI}]$  and  $[\text{EMIM}][\text{TFSI}]$  mixed

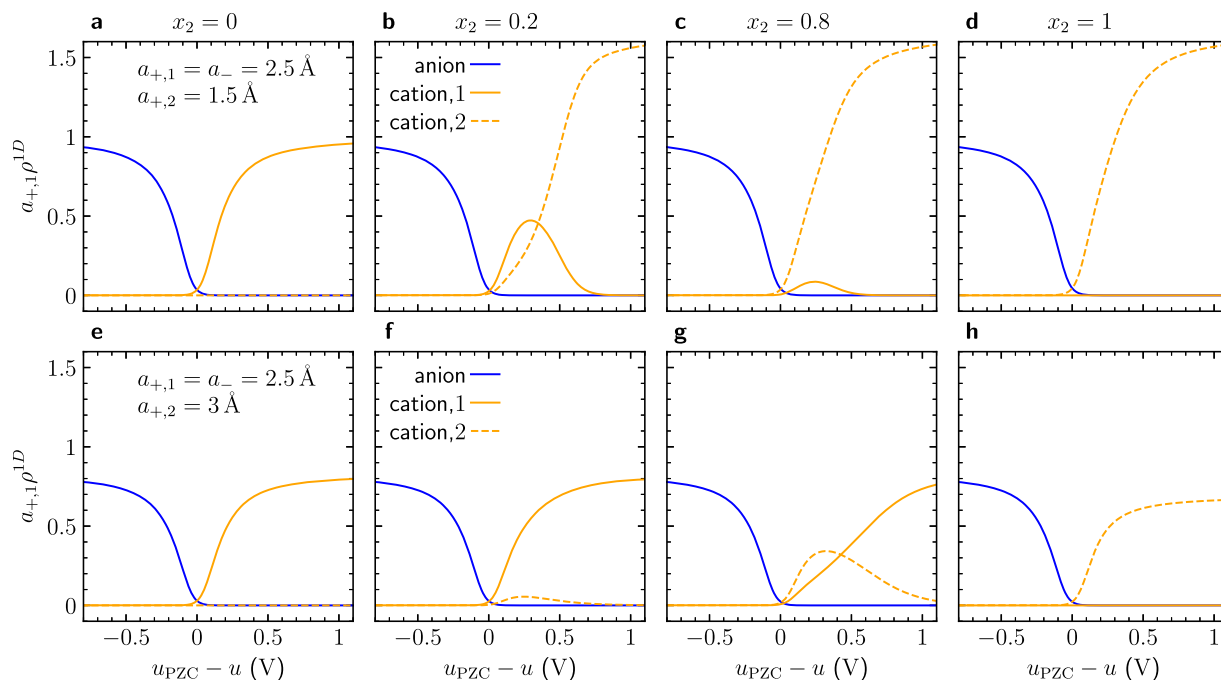


**Fig. 2. Voltage dependence of ion densities inside a nanotube.** An electrolyte consists of anions of radius  $a_- = 2.5 \text{ \AA}$  and two types of cations of radii  $a_{+,1} = 2.5 \text{ \AA}$  and (a-d)  $a_{+,2} = 1.5 \text{ \AA}$  and (e-h)  $a_{+,2} = 3 \text{ \AA}$ . The results are plotted for different values of molar fraction of the second IL  $x_2$ . Temperature  $T = 400 \text{ K}$  and pore radius  $R = 5.6 \text{ \AA}$ .  $u_{PZC}$  is the potential of zero charge.

with [K][TFSI] (Section 3.4). In Section 3.5, we discuss the role of pore size distribution in charge storage and how to match it with an IL mixture to enhance capacitive energy storage.

### 3.1. Charging a single nanopore

The equilibrium ion densities inside a nanopore are determined—among other parameters—by the bulk chemical potentials of ion pairs  $\tilde{\mu}_i^{3D}$ , where  $i$  denotes an ion pair. As described in Section 2.1.1, we computed  $\tilde{\mu}_i^{3D}$  for two cases: (i) when the total ion concentration and (ii) the pressure of a bulk electrolyte is kept constant when varying the molar fraction  $x_2$  of the second IL (case (i) implies the presence of a solvent, assumed implicit in this work). In both cases, we obtained qualitatively similar results. We discuss here the constant pressure case and show the results for the constant ion concentration in Supplementary Material (Figs. S4 and S5).

In Fig. 2a-d, we show 1D ion densities  $\rho_\alpha^{1D} = N_\alpha/L$ , where  $N_\alpha$  is the number of particles of type  $\alpha$  and  $L$  is the pore length, as functions of the potential difference  $u$  (measured relative to the potential of zero charge,  $u_{PZC}$ , see Section 2.1.3) for four values of molar fraction  $x_2$  of the second cation, which in these plots is smaller than the cation of the first IL. By increasing  $x_2$  even slightly from zero, the density of the larger cation becomes bell shaped as a function of  $u$ , and its magnitude decreases with increasing  $x_2$ . Conversely, the density of the smaller cation becomes a monotonic function of  $u$  (for  $x_2 > 0$ ) and saturates at a maximum value  $\rho_{\max}^{1D} = 1/a_{+,2}$  at high potentials. Thus, with increasing  $x_2$ , the charging becomes more and more determined by the smaller cation, similarly as for slit mesopores investigated by Cats and van Roij [13].

In contrast, adding to the neat IL an IL featuring a larger cation (i.e., choosing  $a_{+,2} > a_{+,1}$ ) exerts only a minor influence on the ion densities (Fig. 2e-h). In this case, the density of the added cation has a bell shape as a function of  $u$ , while the density of the first (smaller) cation remains monotonic for all molar fractions  $x_2 < 1$ . This result aligns with the conclusion that nanopore charging is predominantly governed by the smaller cations.

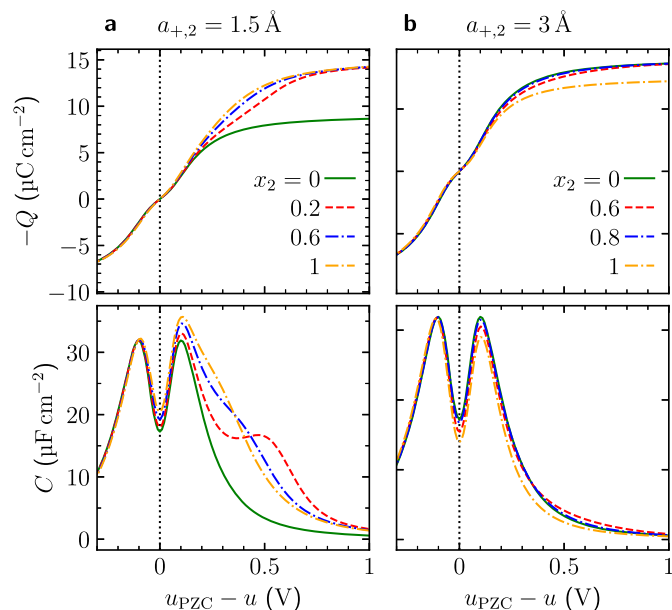


**Fig. 3. Charging a nanotube with binary cation IL mixtures.** An electrolyte consists of anions of radius  $a_- = 2.5 \text{ \AA}$  and two types of cations of radii  $a_{+,1} = 2.5 \text{ \AA}$  and (a)  $a_{+,2} = 1.5 \text{ \AA}$  and (b)  $a_{+,2} = 3 \text{ \AA}$ . Electrode charge (top plots) and capacitance (bottom plots) are plotted for different values of molar fraction of the second ion pair  $x_2$ . Temperature  $T = 400 \text{ K}$  and pore radius  $R = 5.6 \text{ \AA}$ .  $u_{PZC}$  is the potential of zero charge.

These differences in ion densities become evident in the charge and capacitance behaviour, which we illustrate in Fig. 3. For  $u_{PZC} - u > 0$ , adding an IL with a smaller cation ( $a_{+,2} < a_{+,1}$ ) results in an augmentation of accumulated charge and the corresponding enhancement in capacitance (Fig. 3a). At high negative potentials, the maximum capacitance is attained at approximately  $x_2 \approx 0.2$ , indicating a non-monotonic dependence on  $x_2$ . Consistent with the observations from Fig. 2e-h, mix-

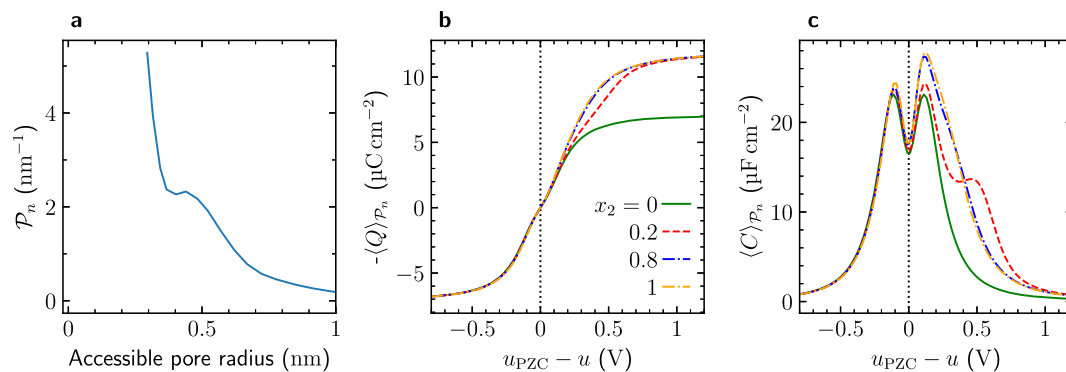


**Fig. 4. Charging a nanoporous electrode.** (a) Normalised distribution of the number of pores,  $\mathcal{P}_n$ , determined for the activated carbon black (Fig. 1) using Eq. (8) and assuming cylindrical pores. (b) Averaged accumulated charge and (c) capacitance per surface area as functions of the potential difference applied to the electrode relative to the potential of zero charge,  $u_{\text{PZC}}$ . The averaging over the distribution of pores has been performed using Eq. (9) and the PSD from panel (a). An electrolyte is a mixture of anions of radius  $a_- = 2.5 \text{ \AA}$  and of two types of cations of radii  $a_{+,1} = 2.5 \text{ \AA}$  and  $a_{+,2} = 1.5 \text{ \AA}$ .  $x_2$  denotes the molar fraction of the smaller cations. Temperature  $T = 400 \text{ K}$ .

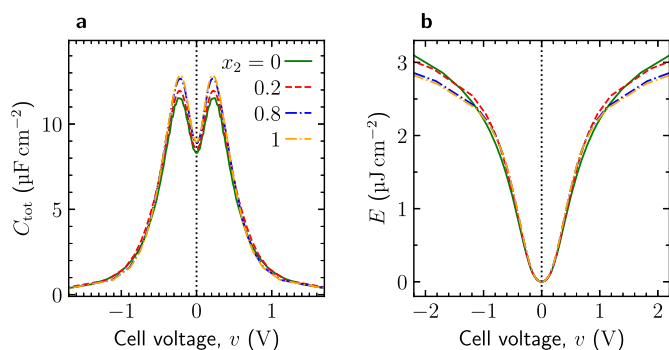


**Fig. 5. Charging a symmetric EDLC.** (a) Total capacitance  $C_{\text{tot}}$  of a two-electrode cell obtained as described in Section 2.1.5.  $C_{\text{tot}}$  is plotted as a function of the cell voltage  $v$ . (b) Stored energy density (Eq. (14)) as a function of the cell voltage. Parameters are the same as in Fig. 4.

ing a symmetric IL with an IL containing a larger cation yields only a marginal impact on charge storage and capacitance, as indicated in Fig. 3b. Henceforth, we consider IL mixtures composed of comparably-sized cations and anions with an addition of an IL possessing the same anion and a smaller cation.

### 3.2. Charging a single nanoporous electrode

To study charging of nanoporous electrodes, we averaged the analytical results for single nanotubes of different radii over the pore size distribution (PSD),  $\mathcal{P}_n$ , of the carbon black used in our experiments. The corresponding distribution of the number of pores, obtained as described in Section 2.1.4, is shown in Fig. 4a.

Fig. 4b shows that for  $u_{\text{PZC}} - u \gtrsim 0.5 \text{ V}$ , the accumulated charge  $\langle Q \rangle_{\mathcal{P}_n}$  increases by about 60% for the IL mixtures compared to the pure IL ( $x_2 = 0$ ). This increase is mainly driven by the charge storage enhancement of single nanopores due to the presence of smaller cations in the mixture (Fig. 3a). Similarly, the capacitance,  $\langle C \rangle_{\mathcal{P}_n}$ , also increases for  $u < u_{\text{PZC}}$  when using the IL mixtures (Fig. 4c). Overall,  $\langle C \rangle_{\mathcal{P}_n}$  has a similar structure as in the case of single nanopores (Fig. 3a) and, in particular, shows a non-monotonic behaviour as a function of  $x_2$ .

### 3.3. Charging a symmetric EDLC

We next calculated the total capacitance ( $C_{\text{tot}}$ ) for a symmetric EDLC consisting of two identical nanoporous electrodes as in Section 3.2. The results are shown in Fig. 5a and demonstrate that, while capacitance increases slightly, the effect is much weaker than for a single electrode

and occurs only in a small voltage window around  $\approx 0.3 \text{ V}$ . This is partially expected, as the EDLC electrodes form two capacitors in series, thus reducing the total capacitance compared to a single electrode. As the voltage increases, the capacitance becomes virtually independent of  $x_2$  and does not show any enhancement. The reason is that the negative electrode (i.e., the electrode with a negative charge on it) does not match the higher charge accumulated in the positive electrode. Thus, a two-electrode symmetric EDLC does not utilize the IL mixture-enhanced performance of the positive electrode. This behaviour is also reflected in the stored energy density,

$$E(v) = \int_0^v v' C_{\text{tot}}(v') dv', \quad (14)$$

which shows only minor changes for the IL mixtures compared to the pure IL.

### 3.4. Charging a symmetric EDLC: experimental results

To verify the validity of our theoretical predictions, we performed electrochemical experiments in two electrodes PEEK cells examined using cyclic voltammetry (CV), galvanostatic charge/discharge (GC/GD), and electrochemical impedance spectroscopy (EIS). Fig. 6a-b show the cyclic voltammograms (at  $5 \text{ mV s}^{-1}$ ) and galvanostatic charge/discharge (at  $200 \text{ mA g}^{-1}$ ) up to  $3 \text{ V}$  with neat [EMIM][TFSI] and  $[\text{K}]_{0.1}[\text{EMIM}]_{0.9}$ -[TFSI] electrolytes. The cyclic voltammograms of the two cells display rectangular shapes (Fig. 6a) and the GC/GD has a triangular shape characteristic of charging an electrical double-layer [53].

At a specific current of  $200 \text{ mA g}^{-1}$  (Fig. 6b), the two cells displayed almost comparable specific capacitance values of  $(122 \pm 5) \text{ F g}^{-1}$  and  $(118 \pm 5) \text{ F g}^{-1}$  for the capacitors using [EMIM][TFSI] and  $[\text{K}]_{0.1}[\text{EMIM}]_{0.9}$ [TFSI] electrolytes, respectively. Previous works reported comparable capacitance values for supercapacitors in organic electrolytes using the same carbon as studied in this work [54,55]. At lower scanning rates of  $2 \text{ mV s}^{-1}$  and  $5 \text{ mV s}^{-1}$  (Fig. 6c), the cell using the neat [EMIM][TFSI] demonstrates a slightly higher capacitance value than the cells made with  $[\text{K}]_{0.1}[\text{EMIM}]_{0.9}$ [TFSI] electrolyte. Moreover, the potassium-containing IL showed an energy efficiency of 97%, whereas the cell with neat [EMIM][TFSI] provided a slightly higher value of 99%. Compared to the cell made with  $[\text{K}]_{0.1}[\text{EMIM}]_{0.9}$ [TFSI] electrolyte, the relatively higher capacitance and efficiency value of the cell with neat [EMIM][TFSI] at lower rates can be linked to the lower viscosity of the neat electrolyte, which facilitates ions mobility within the pores of the carbon electrode material [53].

The electrochemical impedance spectroscopy data (Fig. 6d-f) confirm a better electrochemical performance for the cells made of pure [EMIM][TFSI], as evidenced by the low-frequency region of its Nyquist

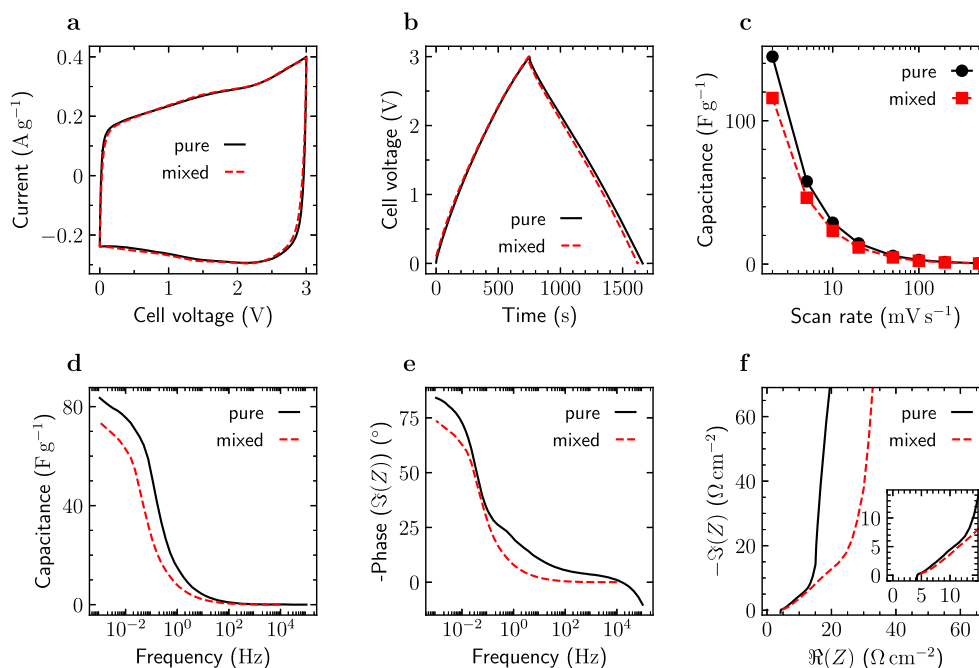


**Fig. 6.** Experimental results for EDLCs with pure [EMIM][TFSI] and its 9:1 mixture with [K][TFSI]. (a) CV curves at a scan rate of 5 mV s<sup>-1</sup> and (b) GC/GD curves at a specific current of 200 mA g<sup>-1</sup>. Specific capacitances as a function of (c) scanning rate and (d) frequency. (e) Bode plot and (f) Nyquist plot obtained in the frequency range from 100 kHz to 1 MHz.

plot being more parallel to the imaginary axis (Fig. 6f). The potassium-based cell data demonstrate lower capacitance values (Fig. 6d) and lower phase angles (Fig. 6e) versus frequency. The phase angle at a frequency of 1 MHz is 84° for the pure [EMIM][TFSI] compared to 81° for the [K]<sub>0.1</sub>[EMIM]<sub>0.9</sub>[TFSI] cell. The time constant calculated at 45° phase angle is 19.2 s and 43.5 s for the device made with [EMIM][TFSI] and [K]<sub>0.1</sub>[EMIM]<sub>0.9</sub>[TFSI] electrolyte, respectively. In the high-frequency region of the Nyquist plots (Fig. 6f), the device using the neat ionic liquid electrolyte revealed a lower ionic resistance ( $R_i$ ) than the cell with the mixed electrolyte. The obtained  $R_i$  is 0.38 Ω cm<sup>2</sup> and 0.49 Ω cm<sup>2</sup> for the device made with [EMIM][TFSI] and [K]<sub>0.1</sub>[EMIM]<sub>0.9</sub>[TFSI] electrolytes, respectively. Thus, adding potassium salt increases the electrolytes' viscosity due to the interaction between [K]<sup>+</sup> and [TFSI]<sup>-</sup> ions [56], influencing the ion transport within the pores [57].

### 3.5. Can IL mixtures enhance energy storage?

Our theoretical calculations and electrochemical experiments showed that the binary cation IL mixtures used in this work did not substantially enhance capacitance (and even lowered it) compared to the neat IL (Figs. 5 and 6). To understand this result, we analysed the distribution of pores in the activated carbon black used in the calculations and experiments. By integrating the corresponding PSD computed for slit pores (Fig. S3) and using the average dimension of [EMIM]<sup>+</sup> cation ( $\approx 0.37$  nm), we estimated that about 86 % of pores are accessible to all cations and about 14 % of pores are accessible only to the potassium ion (radius 0.28 nm). Thus, the percentage of pores accessible to the potassium cation and inaccessible to the [EMIM]<sup>+</sup> cation was relatively small and even those pores were likely not fully utilized during charging with high scan rates used in our experiments, explaining the negligible effect of using [K]<sub>0.1</sub>[EMIM]<sub>0.9</sub>[TFSI] mixture (Fig. 6).

To get deeper insights into the interplay between pore-size distribution and ion sizes and how they relate to capacitance and energy storage, we carried out theoretical calculations for a model electrode generated in a computer [58] using Gaussian random fields [59,60]. This model electrode reproduces well the SAXS intensity and the distribution of pore sizes of titanium carbide-derived carbons chlorinated at

600 °C (CDC600) [61]. Fig. 7a shows a PSD of the CDC600 electrode assuming cylindrical pores. For our model IL mixture, we estimated that about 51 % of the CDC600 pores are accessible to all ions (pore radii above 0.25 nm) and 49 % are accessible only to the smallest cation in the mixture (radius 0.15 nm). The abundance of such narrow pores makes the IL mixture work more efficiently and enhance the capacitance much more substantially than in the case of the activated carbon black (compare Fig. 7b with Fig. 4c).

Consequently, the binary cation electrolytes deliver elevated capacitances and stored energy densities also with two-electrode cells, albeit only under low and intermediate cell voltages, as depicted in Fig. 7c,d. At higher voltages (above approximately 0.8 V), the enhanced performance of the positive electrode encounters constraints imposed by the negative electrode, whose subnanometer pores remain unoccupied because of bulky anions. This observation suggests that the energy stored by EDLCs can be increased by incorporating quaternary electrolytes comprising dual anionic and cationic species or by deploying asymmetric electrodes featuring different pore size distributions to counterbalance the charge accumulation on the electrodes.

## 4. Conclusions

We have explored IL mixtures comprising a shared anion and two distinct cations of varying sizes, scrutinizing the interplay between these IL mixtures and nanoporous electrodes concerning capacitive energy storage. Our theoretical approach involved a model of electrolyte-filled single-file pores, which we mapped onto a one-dimensional, off-lattice model endowed with an exact analytical solution, allowing us to systematically investigate the relationship among the electrolyte, porous electrode, and capacitance. The investigation showed that adding an IL featuring a small cation to an IL containing bulky ions can substantially augment the capacitance of single nanopores and nanoporous electrodes when subject to negative potential differences relative to the potential of zero charge (Fig. 4). We found a non-monotonic relationship between capacitance and the relative concentration of ILs in the mixture (Figs. 3 and 4). However, this non-monotonic behaviour ceased to manifest in nanoporous electrodes characterized by

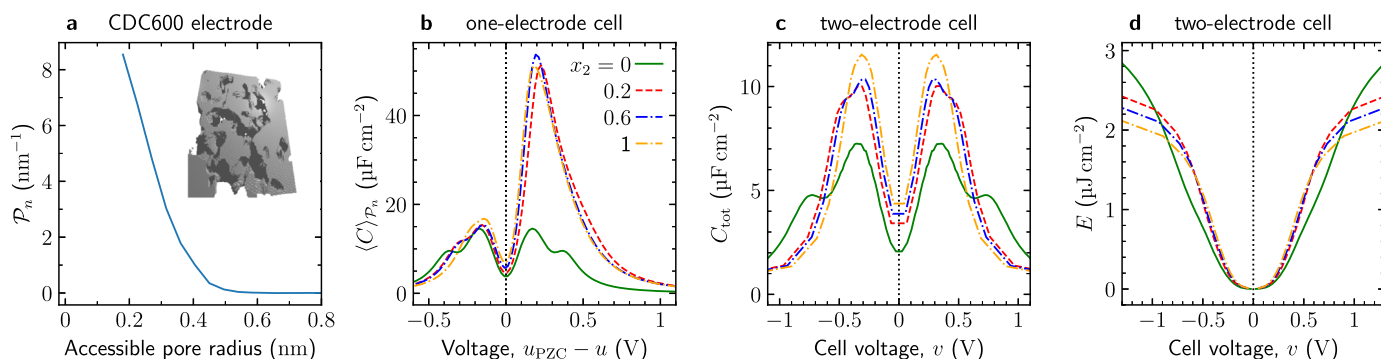


**Fig. 7. Charging a symmetric EDLCs with model CDC600 electrodes.** (a) Normalised distribution of the number of pores determined for model CDC600 electrodes using Eq. (8) and the volumetric pore-size distribution (PSD) from Ref. [58]. The inset shows a 3D illustration of the CDC600 pore structure. (b) Average capacitance per surface area as a function of the potential difference applied to the electrode relative to the potential of zero charge,  $u_{PZC}$ . The averaging has been performed using Eq. (9) and the PSD from panel (a). (c) Total capacitance  $C_{tot}$  of a two-electrode cell obtained as described in Section 2.1.5.  $C_{tot}$  is plotted as a function of the cell voltage  $v$ . (d) Stored energy density as a function of cell voltage. An electrolyte is a mixture of anions of radius  $a_- = 2.5 \text{ \AA}$  and of two types of cations of radii  $a_{+,1} = 2.5 \text{ \AA}$  and  $a_{+,2} = 1.5 \text{ \AA}$ . Temperature  $T = 400 \text{ K}$ .

an abundance of micropores and in two-electrode EDLC devices (Figs. 5 and 7).

In the case of EDLCs, our findings indicated a weaker capacitance enhancement when employing binary cation electrolytes compared to single electrodes (Figs. 5 and 7). Particularly at elevated cell voltages, the neat IL exhibited superior performance over binary cation IL mixtures. This result can be attributed to the limitations of the EDLC's performance by one of its electrodes, whose narrow pores could not be optimally utilized due to the presence of sizable anions. Our electrochemical experiments followed similar trends, demonstrating comparable capacitances for neat [EMIM][TFSI] and for its mixture with [K][TFSI] (Fig. 6). Slight enhancements in cell properties with the use of [EMIM][TFSI], compared to the potassium-containing cell, likely stem from the lower conductivity of the mixed electrolyte.

#### CRedit authorship contribution statement

**Anna Seltmann:** Data curation, Investigation, Visualization, Writing – original draft. **Taras Verkholyak:** Conceptualization, Data curation, Investigation, Methodology, Software, Validation, Writing – original draft. **Dariusz Gołowicz:** Data curation, Investigation, Software, Writing – review & editing. **Emmanuel Pameté:** Data curation, Investigation, Methodology, Visualization, Writing – review & editing. **Andrij Kuzmak:** Conceptualization, Data curation, Investigation, Writing – review & editing. **Volker Presser:** Funding acquisition, Supervision, Validation, Writing – review & editing. **Svyatoslav Kondrat:** Conceptualization, Funding acquisition, Investigation, Methodology, Project administration, Supervision, Validation, Visualization, Writing – original draft.

#### Declaration of competing interest

The authors declare that they have no known competing financial interests or personal relationships that could have appeared to influence the work reported in this paper.

#### Data availability

Data will be made available on request.

#### Acknowledgements

S.K. is immensely grateful to Professor Myroslav Holovko for his invaluable mentorship during the formative stages of his career, as well as for the unwavering support, keen interest, and countless insightful scientific and general discussions that have persisted over time. We

thank Jonas Landsgesell and David Beyer (Institute for Computational Physics, Stuttgart University) for their help with Espresso simulations and the Widom insertion method. This work was supported by NCN grant No. 2020/39/1/ST3/02199 to S.K. and D.G. and by DFG grant No. PR-1173/27 to A.S., E.P. and V.P. within the joint Polish-German project SUPILMIX. We thank David Aradilla for the help with the preparation of the SUPILMIX proposal. S.K. was supported by NCN grant No. 2021/40/Q/ST4/00160. E.P. acknowledges the financial support from the Alexander von Humboldt Foundation.

#### Appendix A. Supplementary material

Supplementary material related to this article can be found online at <https://doi.org/10.1016/j.molliq.2023.123369>.

#### References

- [1] J.R. Miller, P. Simon, Electrochemical capacitors for energy management, *Science* 321 (2008) 651.
- [2] A. González, E. Goikolea, J.A. Barrena, R. Mysyk, Review on supercapacitors: technologies and materials, *Renew. Sustain. Energy Rev.* 58 (2016) 1189.
- [3] G. Jeanmaret, B. Rotenberg, M. Salanne, Microscopic simulations of electrochemical double-layer capacitors, *Chem. Rev.* 122 (2022) 10860.
- [4] S. Kondrat, G. Feng, F. Bresme, M. Urbakh, A.A. Kornyshev, Theory and simulations of ionic liquids in nanoconfinement, *Chem. Rev.* 123 (2023) 6668.
- [5] M. Janssen, A. Härtel, R. van Roij, Boosting capacitive blue-energy and desalination devices with waste heat, *Phys. Rev. Lett.* 113 (2014) 268501.
- [6] A. Härtel, M. Janssen, D. Weingarth, V. Presser, R. Van Roij, Heat-to-current conversion of low-grade heat from a thermocapacitive cycle by supercapacitors, *Energy Environ. Sci.* 8 (2015) 2396.
- [7] I. Atlas, G.Z. Ramon, Periodic energy conversion in an electric-double-layer capacitor, *J. Colloid Interface Sci.* 530 (2018) 675.
- [8] H. Kim, J. Kim, S. Hoon Kim, J. Hun Seol, Continuous power production using flowable electrodes based on waste-heat assisted capacitive mixing, *Appl. Therm. Eng.* 206 (2022) 118094.
- [9] M. Janssen, T. Verkholyak, A. Kuzmak, S. Kondrat, Optimising nanoporous supercapacitors for heat-to-electricity conversion, *J. Mol. Liq.* 371 (2023) 121093.
- [10] P. Simon, Y. Gogotsi, Perspectives for electrochemical capacitors and related devices, *Nat. Mater.* 19 (2020) 1151.
- [11] X. Wang, A.Y. Mehandzhyski, B. Arstad, K.L. Van Aken, T.S. Mathis, A. Gallegos, Z. Tian, D. Ren, E. Sheridan, B.A. Grimes, D.-e. Jiang, J. Wu, Y. Gogotsi, D. Chen, Selective charging behavior in an ionic mixture electrolyte-supercapacitor system for higher energy and power, *J. Am. Chem. Soc.* 139 (2017) 18681.
- [12] J.N. Neal, D.J. Wesolowski, D. Henderson, J. Wu, Electric double layer capacitance for ionic liquids in nanoporous electrodes: effects of pore size and ion composition, *J. Mol. Liq.* 270 (2018) 145.
- [13] P. Cats, R. van Roij, The differential capacitance as a probe for the electric double layer structure and the electrolyte bulk composition, *J. Chem. Phys.* 155 (2021) 104702.
- [14] E.P. Yambou, B. Gorska, F. Béguin, Electrical double-layer capacitors based on a ternary ionic liquid electrolyte operating at low temperature with realistic gravimetric and volumetric energy outputs, *ChemSusChem* 14 (2021) 1196.

- [15] T. Verkholyak, A. Kuzmak, S. Kondrat, Capacitive energy storage in single-file pores: exactly solvable models and simulations, *J. Chem. Phys.* 155 (2021) 174112.
- [16] J. Landers, G.Y. Gor, A.V. Neimark, Density functional theory methods for characterization of porous materials, *Colloids Surf. A, Physicochem. Eng. Asp.* 437 (2013) 3.
- [17] D. Di Caprio, M. Valiskó, M. Holovko, D. Boda, Anomalous temperature dependence of the differential capacitance in valence asymmetric electrolytes. Comparison of Monte Carlo simulation results and the field theoretical approach, *Mol. Phys.* 104 (2006) 3777.
- [18] S. Kondrat, N. Georgi, M.V. Fedorov, A.A. Kornyshev, A superionic state in nanoporous double-layer capacitors: insights from Monte Carlo simulations, *Phys. Chem. Chem. Phys.* 13 (2011) 11359.
- [19] S. Kondrat, C.R. Pérez, V. Presser, Y. Gogotsi, A.A. Kornyshev, Effect of pore size and its dispersity on the energy storage in nanoporous supercapacitors, *Energy Environ. Sci.* 5 (2012) 6474.
- [20] D.-e. Jiang, J. Wu, Microscopic insights into the electrochemical behavior of non-aqueous electrolytes in electric double-layer capacitors, *J. Phys. Chem. Lett.* 4 (2013) 1260.
- [21] M.F. Holovko, O. Patsahan, T. Patsahan, Vapour-liquid phase diagram for an ionic fluid in a random porous medium, *J. Phys. Condens. Matter* 28 (2016) 414003.
- [22] M.F. Holovko, T.M. Patsahan, O.V. Patsahan, Application of the ionic association concept to the study of the phase behaviour of size-asymmetric ionic fluids in disordered porous media, *J. Mol. Liq.* 235 (2017) 53.
- [23] Y.V. Kalyuzhnyi, J. Rešič, M. Holovko, P.T. Cummings, Primitive models of room temperature ionic liquids. Liquid-gas phase coexistence, *J. Mol. Liq.* 270 (2018) 7.
- [24] O. Patsahan, T. Patsahan, M. Holovko, Vapour-liquid critical parameters of a 2:1 primitive model of ionic fluids confined in disordered porous media, *J. Mol. Liq.* 270 (2018) 97.
- [25] M. Hvozď, T. Patsahan, O. Patsahan, M. Holovko, Fluid-fluid phase behaviour in the explicit solvent ionic model: hard spherocylinder solvent molecules, *J. Mol. Liq.* 285 (2019) 244.
- [26] M. Hvozď, O. Patsahan, T. Patsahan, M. Holovko, Fluid-fluid phase behaviour in the explicit hard spherocylinder solvent ionic model confined in a disordered porous medium, *J. Mol. Liq.* 346 (2022) 117888.
- [27] J.N. Neal, K.L. Van Aken, Y. Gogotsi, D.J. Wesolowski, J. Wu, Self-amplified surface charging and partitioning of ionic liquids in nanopores, *Phys. Rev. Appl.* 8 (2017) 034018.
- [28] J.N. Neal, D.J. Wesolowski, D. Henderson, J. Wu, Ion distribution and selectivity of ionic liquids in microporous electrodes, *J. Chem. Phys.* 146 (2017) 174701.
- [29] B. Widom, Some topics in the theory of fluids, *J. Chem. Phys.* 39 (2004) 2808.
- [30] F. Weik, R. Weeber, K. Szuttor, K. Breitsprecher, J. de Graaf, M. Kuron, J. Lands-gesell, H. Menke, D. Sean, C. Holm, ESPResSo 4.0 – an extensible software package for simulating soft matter systems, *Eur. Phys. J. Spec. Top.* 227 (2019) 1789, arXiv:1811.07729 [cond-mat, physics:physics].
- [31] A.C. Forse, C. Merlet, J.M. Griffin, C.P. Grey, New perspectives on the charging mechanisms of supercapacitors, *J. Am. Chem. Soc.* 138 (2016) 5731.
- [32] J. Jover, A.J. Haslam, A. Galindo, G. Jackson, E.A. Müller, Pseudo hard-sphere potential for use in continuous molecular-dynamics simulation of spherical and chain molecules, *J. Chem. Phys.* 137 (2012) 144505.
- [33] A.P. Thompson, H.M. Aktulga, R. Berger, D.S. Bolinteanu, W.M. Brown, P.S. Crozier, P.J. in 't Veld, A. Kohlmeyer, S.G. Moore, T.D. Nguyen, R. Shan, M.J. Stevens, J. Tranchida, C. Trott, S.J. Plimpton, LAMMPS - a flexible simulation tool for particle-based materials modeling at the atomic, meso, and continuum scales, *Comput. Phys. Commun.* 271 (2022) 108171.
- [34] T. Verkholyak, A. Kuzmak, A.A. Kornyshev, S. Kondrat, Less is more: can low quantum capacitance boost capacitive energy storage?, *J. Phys. Chem. Lett.* 13 (2022) 10976.
- [35] S. Kondrat, A. Kornyshev, Superionic state in double-layer capacitors with nanoporous electrodes, *J. Phys. Condens. Matter* 23 (2010) 022201.
- [36] B. Skinner, T. Chen, M.S. Loth, B.I. Shklovskii, Theory of volumetric capacitance of an electric double-layer supercapacitor, *Phys. Rev. E* 83 (2011) 056102.
- [37] C.C. Rochester, A.A. Lee, G. Pruessner, A.A. Kornyshev, Interionic interactions in conducting nanoconfinement, *ChemPhysChem* 14 (2013) 4121.
- [38] A.A. Lee, S. Kondrat, A.A. Kornyshev, Single-file charge storage in conducting nanopores, *Phys. Rev. Lett.* 113 (2014) 048701.
- [39] A. Goduljan, F. Juarez, L. Mohammadzadeh, P. Quaino, E. Santos, W. Schmickler, Screening of ions in carbon and gold nanotubes — a theoretical study, *Electrochem. Commun.* 45 (2014) 48.
- [40] L. Mohammadzadeh, A. Goduljan, F. Juarez, P. Quaino, E. Santos, W. Schmickler, Nanotubes for charge storage – towards an atomistic model, *Electrochim. Acta* 162 (2015) 11.
- [41] L. Mohammadzadeh, P. Quaino, W. Schmickler, Interactions of anions and cations in carbon nanotubes, *Faraday Discuss.* 193 (2016) 415.
- [42] S. Luryi, Quantum capacitance devices, *Appl. Phys. Lett.* 52 (1988) 501.
- [43] H. Gerischer, An interpretation of the double layer capacity of graphite electrodes in relation to the density of states at the Fermi level, *J. Phys. Chem.* 89 (1985) 4249.
- [44] H. Ji, X. Zhao, Z. Qiao, J. Jung, Y. Zhu, Y. Lu, L.L. Zhang, A.H. MacDonald, R.S. Ruoff, Capacitance of carbon-based electrical double-layer capacitors, *Nat. Commun.* 5 (2014) 3317.
- [45] D. Weingarth, M. Zeiger, N. Jäckel, M. Aslan, G. Feng, V. Presser, Graphitization as a universal tool to tailor the potential-dependent capacitance of carbon supercapacitors, *Adv. Energy Mater.* 4 (2014) 1400316.
- [46] J. Li, P.J. Burke, Measurement of the combined quantum and electrochemical capacitance of a carbon nanotube, *Nat. Commun.* 10 (2019) 3598.
- [47] F. Aikebaier, A. Pertsova, C.M. Canali, Effects of short-range electron-electron interactions in doped graphene, *Phys. Rev. B* 92 (2015) 155420.
- [48] H. Longuet-Higgins, One-dimensional multicomponent mixtures, *Mol. Phys.* 1 (1958) 83.
- [49] K. Meyer, P. Klobes, Comparison between different presentations of pore size distribution in porous materials, *Fresenius J. Anal. Chem.* 363 (1999) 174.
- [50] L.D. Gelb, K.E. Gubbins, Pore size distributions in porous glasses: a computer simulation study, *Langmuir* 15 (1999) 305.
- [51] P. Pfeifer, G.P. Johnston, R. Deshpande, D.M. Smith, A.J. Hurd, Structure analysis of porous solids from preadsorbed films, *Langmuir* 7 (1991) 2833.
- [52] H. Shim, Ö. Budak, V. Haug, M. Widmaier, V. Presser, Comparison of organic electrolytes at various temperatures for 2.8 V-Li-ion hybrid supercapacitors, *Electrochim. Acta* 337 (2020) 135760.
- [53] E. Pamaté, B. Gorska, V. Pavlenko, F. Béguin, Fitting the porous texture of carbon electrodes to a binary ionic liquid electrolyte for the realization of low temperature EDLCs, *Electrochim. Acta* 350 (2020) 136416.
- [54] N. Jäckel, D. Weingarth, A. Schreiber, B. Krüner, M. Zeiger, A. Tolosa, M. Aslan, V. Presser, Performance evaluation of conductive additives for activated carbon supercapacitors in organic electrolyte, *Electrochim. Acta* 191 (2016) 284.
- [55] R.E. Ruther, C.-N. Sun, A. Holliday, S. Cheng, F.M. Delnick, T.A. Zawodzinski, J. Nanda, Stable electrolyte for high voltage electrochemical double-layer capacitors, *J. Electrochem. Soc.* 164 (2016) A277.
- [56] M. Kerner, N. Plylahan, J. Scheers, P. Johansson, Ionic liquid based lithium battery electrolytes: fundamental benefits of utilising both TFSI and FSI anions?, *Phys. Chem. Chem. Phys.* 17 (2015) 19569.
- [57] E. Pamaté, B. Gorska, F. Béguin, Binary mixtures of ionic liquids based on EMIm cation and fluorinated anions: physico-chemical characterization in view of their application as low-temperature electrolytes, *J. Mol. Liq.* 298 (2020) 111959.
- [58] O.A. Vasilyev, A.A. Kornyshev, S. Kondrat, Connections matter: on the importance of pore percolation for nanoporous supercapacitors, *ACS Appl. Energy Mater.* 2 (2019) 5386.
- [59] N.F. Berk, Scattering properties of a model bicontinuous structure with a well defined length scale, *Phys. Rev. Lett.* 58 (1987) 2718.
- [60] C.J. Gommès, A.P. Roberts, Structure development of resorcinol-formaldehyde gels: microphase separation or colloid aggregation, *Phys. Rev. E* 77 (2008) 041409.
- [61] C. Prehal, C. Koczwara, N. Jäckel, A. Schreiber, M. Burian, H. Amenitsch, M.A. Hartmann, V. Presser, O. Paris, Quantification of ion confinement and desolvation in nanoporous carbon supercapacitors with modelling and in situ X-ray scattering, *Nat. Energy* 2 (2017) 1.